Prepared for submission to JINST

Characterization of the Hamamatsu photomultipliers for Phase 1 of KM3NeT

M. Ageron,[b] S. Aiello,[s] F. Ameli,[w] E. G. Anassontzis,[aa] M. Andre,[aq] G. Androulakis,[ac] M. Anghinolfi,[t] G. Anton,[h] M. Ardid,[ar] J. Aublin,[at] T. Avgitas,[at] M. Baars,[g] C. Bagatelas,[ac] G. Barbarino,[u,am] E. Barbarito,[q] B. Baret,[at] J. Barrios-Martí,[m] A. Belias,[ac] E. Berbee,[g] A. van den Berg,[k] V. Bertin,[b] S. Beurthey,[b] V. van Beveren,[g] N. Beverini,[an,v] S. Biagi,[o] A. Biagioni,[w] C. Biernoth,[h] M. Billault,[b] R. de Boer,[g] M. Bondì,[s] R. Bormuth,[g,y] B. Bouhadef,[v] G. Bourlis,[l] S. Bourret,[at] C. Boutonnet,[at] M. Bouwhuis,[g] C. Bozza,[ao] H.Brânzaş,[x] N. Briukhanova,[t] R. Bruijn,[av] J. Brunner,[b] E. Buis,[ag] R. Buompane,[u,aj] J. Busto,[b] G. Cacopardo,[o] L. Caillat,[b] M. Calamai,[v] D. Calvo,[m] G. Cannizzaro,[o] A. Capone,[ap,w] L. Caramete,[x] H. Carduner,[ae] S. Cecchini,[r] S. Celli,[ap,w,j] A. Ceres,[q] M. Chabab,[d] C. Champion,[at] S. Cherubini,[o,aw] V. Chiarella,[p] T. Chiarusi,[r] M. Circella,[q] D. Cobas,[at] R. Cocimano,[o] J. A. B. Coelho,[at] A. Coleiro,[m] R. Coletti,[b] M. Colomer Molla,[at,m] S. Colonges,[at] R. Coniglione,[o] A. Cosquer,[b] P. Coyle,[b] A. Creusot,[at] G. Cuttone,[o] C. D'Amato,[o] A. D'Amico,[g] A. D'Onofrio,[u,aj] R. Dallier,[ae] T. Damianos,[ac] C. De Sio,[ao] I. Di Palma,[ap,w] Antonio F. Díaz,[ai] C. Distefano,[o] A. Domi,[t,al] R. Donà,[r,ak] C. Donzaud,[at] D. Dornic,[b] Q. Dorosti-Hasankiadeh,[k] M. Dörr,[az] M. Durocher,[o,j] T. Eberl,[h] D. van Eijk,[g] I. El Bojaddaini,[au] D. Elsaesser,[az] A. Enzenhöfer,[b] G. Ferrara,[o,aw] G. Frascadore,[o] M. Furini,[r] L. A. Fusco,[r,ak] D. Gajana,[g] T. Gal,[h] F. Garufi,[u,am] S. Gauchery,[at] M. Gebyehu,[g] S. Geißelsöder,[h] L. Gialanella,[u,aj] V. Giordano,[s] A. Giuliante,[ay] N. Gizani,[l] N. de Graaf,[g] R. Gracia,[n] R. Gracia Ruiz,[n] K. Graf,[h] D. Grasso,[v] T. Grégoire,[at] G. Grella,[ao] A. Grmek,[o] M. Guerzoni,[r] S. Hallmann,[h] H. van Haren,[ad] S. Harissopulos,[ac] T. Heid,[h] A. Heijboer,[g] E. Heine,[g] A. Hekalo,[az] S. Henry,[b] J. J. Hernández-Rey,[m] J. Hofestädt,[h] G. Illuminati,[m] C. W. James,[h] P. Jansweijer,[g] M. Jongen,[g] B. Jongewaard,[av] M. de Jong,[g] P. de Jong,[g,av] M. Kadler,[az] O. Kalekin,[h] U. F. Katz,[h] F. Kayzel,[g] P. Keller,[b] N. R. Khan Chowdhury,[m] G. Kieft,[g] D. Kießling,[h] S. Kihel,[n] E. N. Koffeman,[g] P. Kooijman,[av,ba] A. Kouchner,[at] M. Kreter,[az] V. Kulikovskiy,[b] R. Lahmann,[h] P. Lamare,[b] G. Larosa,[o] A. Leisos,[l] F. Leone,[o,aw] E. Leonora,[s] G. Levi,[r,ak] M. Lincetto,[b] M. Lindsey Clark,[at] A. Liolios,[c] P. Litrico,[o] C. D. Llorens Alvarez,[ar] D. Lo Presti,[s] H. Löhner,[k] A. Lonardo,[w] M. Lotze,[m] S. Loucatos,[at,e] E. Maccioni,[an,v] G. Maggi,[b] J. Ma?czak,[ab] K. Mannheim,[az] A. Margiotta,[r,ak] A. Margotti,[r] A. Marinelli,[an,v] O. Mariş,[x] C. Markou,[ac] L. Martin,[ae] J. A. Martínez-Mora,[ar] A. Martini,[p] F. Marzaioli,[u,aj] O. Mbeumou,[b] R. van der Meer,[g] R. Mele,[u,am] K. W. Melis,[g] T. Michael,[g] P. Migliozzi,[u] E. Migneco,[o] P. Mijakowski,[ab] A. Miraglia,[o] C. M. Mollo,[u] M. Mongelli,[q] M. Morganti,[v,a] M. Moser,[h] A. Moussa,[au] R. Muller,[ag] P. Musico,[t] M. Musumeci,[o] L. Nauta,[g] S. Navas,[ah] C. A. Nicolau,[w] C. Nielsen,[at] M. Organokov,[as] A. Orlando,[o] V. Panagopoulos,[ac] A. Paolucci,[r] A. Papaikonomou,[l] G. Papalashvili,[af] R. Papaleo,[o] G. E. Păvălaş,[x] H. Peek,[g]

G. Pellegrini,[r] C. Pellegrino,[r,ak] P. Piattelli,[o] K. Pikounis,[ac] O. Pisanti,[u,am] C. Poirè,[t,al] G. E. Poma,[o,aw] V. Popa,[x] M. Post,[av] T. Pradier,[n] F. Pratolongo,[t] G. Pühlhofer,[f] S. Pulvirenti,[o] L. Quinn,[b] F. Raffaelli,[v] N. Randazzo,[s] S. Razzaque,[ax] D. Real,[m] L. Resvanis,[aa] J. Reubelt,[h] G. Riccobene,[o] A. Rovelli,[o] M. Saldaña,[ar] I. Salvadori,[b] D. F. E. Samtleben,[g,y] A. Sánchez Losa,[q] M. Sanguineti,[t] A. Santangelo,[f] D. Santonocito,[o] P. Sapienza,[o] B. Schermer,[av] F. Schimmel,[g] J. Schmelling,[g] V. Sciacca,[o] M. Sedita,[o] J. Seneca,[av] I. Sgura,[q] R. Shanidze,[af] A. Sharma,[an] F. Simeone,[w] A. Sinopoulou,[ac] V. Sipala,[s] B. Spisso,[ao,u] A. Spitaleri,[o] M. Spurio,[r,ak] D. Stavropoulos,[ac] G. Stavropoulos,[ac] J. Steijger,[g] S. M. Stellacci,[ao] B. Strandberg,[g] D. Stransky,[h] T. Stüven,[h] M. Taiuti,[t,al] F. Tatone,[s] Y. Tayalati,[z] F. Terrasi,[u,aj] D. Tézier,[b] S. Theraube,[b] P. Timmer,[g] R. Travaglini,[r] A. Trovato,[o] A. Tsirigotis,[l] S. Tzamarias,[c] E. Tzamariudaki,[ac] D. Tzanetatos,[ac] C. Valieri,[r] B. Vallage,[at] V. Van Elewyck,[at] J. Vermeulen,[g] F. Versari,[r,ak] S. Viola,[o] D. Vivolo,[u,am] M. Volkert,[h] G. Voulgaris,[aa] L. de Waardt,[av] P. Werneke,[g] L. Wiggers,[g] J. Wilms,[i] E. de Wolf,[g,av] D. Zaborov,[b] J. D. Zornoza,[m] J. Zúñiga[m]

[a] *Accademia Navale di Livorno, Viale Italia 72, Livorno, 57100 Italy*

[b] *Aix Marseille Univ, CNRS/IN2P3, CPPM, Marseille, France*

[c] *Aristotle University Thessaloniki, University Campus, Thessaloniki, 54124 Greece*

[d] *Cadi Ayyad University, Physics Department, Faculty of Science Semlalia, Av. My Abdellah, P.O.B. 2390, Marrakech, 40000 Morocco*

[e] *CEA, Irfu/SPP, Route Nationale, Gif-sur-Yvette, 91191 France*

[f] *Eberhard Karls Universität Tübingen, Institut für Astronomie und Astrophysik, Sand 1, Tübingen, 72076 Germany*

[g] *FOM, Nikhef, PO Box 41882, Amsterdam, 1098 DB Netherlands*

[h] *Friedrich-Alexander-Universität Erlangen-Nürnberg, Erlangen Centre for Astroparticle Physics, Erwin-Rommel-Straße 1, 91058 Erlangen, Germany*

[i] *Friedrich-Alexander-Universität Erlangen-Nürnberg, Remeis Sternwarte, Sternwartstraße 7, 96049 Bamberg, Germany*

[j] *Gran Sasso Science Institute, GSSI, Viale Francesco Crispi 7, L'Aquila, 67100 Italy*

[k] *KVI-CART University of Groningen, Groningen, the Netherlands*

[l] *Hellenic Open University, School of Science / Technology, Natural Sciences, Sahtouri St. / Ag. Andreou St. 16, Patra, 26222 Greece*

[m] *IFIC - Instituto de Física Corpuscular (CSIC - Universitat de València), c/Catedrático José Beltrán, 2, 46980 Paterna, Valencia, Spain*

[n] *IN2P3, IPHC, 23 rue du Loess, Strasbourg, 67037 France, http://www.iphc.cnrs.fr*

[o] *INFN, Laboratori Nazionali del Sud, Via S. Sofia 62, Catania, 95123 Italy*

[p] *INFN, LNF, Via Enrico Fermi, 40, Frascati, 00044 Italy*

[q] *INFN, Sezione di Bari, Via Amendola 173, Bari, 70126 Italy*

[r] *INFN, Sezione di Bologna, v.le C. Berti-Pichat, 6/2, Bologna, 40127 Italy*

[s] *INFN, Sezione di Catania, Via Santa Sofia 64, Catania, 95123 Italy*

[t] *INFN, Sezione di Genova, Via Dodecaneso 33, Genova, 16146 Italy*

[u] *INFN, Sezione di Napoli, Complesso Universitario di Monte S. Angelo, Via Cintia ed. G, Napoli, 80126 Italy*

[v] *INFN, Sezione di Pisa, Largo Bruno Pontecorvo 3, Pisa, 56127 Italy*

[w] *INFN, Sezione di Roma, Piazzale Aldo Moro 2, Roma, 00185 Italy*

[x] *ISS, Atomistilor 409, Măgurele, RO-077125 Romania*
[y] *Leiden University, Leiden Institute of Physics, PO Box 9504, Leiden, 2300 RA Netherlands*
[z] *University Mohammed V in Rabat, Faculty of Sciences, 4 av. Ibn Battouta, B.P. 1014, R.P. 10000 Rabat, Morocco*
[aa] *Physics Department, N. and K. University of Athens, Athens, Greece*
[ab] *National Centre for Nuclear Research, 00-681 Warsaw, Poland*
[ac] *NCSR Demokritos, Institute of Nuclear and Particle Physics, Ag. Paraskevi Attikis, Athens, 15310 Greece*
[ad] *NIOZ (Royal Netherlands Institute for Sea Research) and Utrecht University, PO Box 59, Den Burg, Texel, 1790 AB, the Netherlands*
[ae] *Subatech, 4 rue Alfred Kastler - La Chantrerie, Nantes, BP 20722 44307 France*
[af] *Tbilisi State University, Department of Physics, 3, Chavchavadze Ave., Tbilisi, 0179 Georgia, http://https://www.tsu.ge/en*
[ag] *TNO, Technical Sciences, PO Box 155, Delft, 2600 AD Netherlands, http://www.tno.nl*
[ah] *University of Granada, Dpto. de Física Teórica y del Cosmos & C.A.F.P.E., 18071 Granada, Spain*
[ai] *University of Granada, Dept. of Computer Architecture and Technology/CITIC, 18071 Granada, Spain*
[aj] *Università degli Studi della Campania "Luigi Vanvitelli", Dipartimento di Matematica e Fisica, viale Lincoln 5, Caserta, 81100 Italy*
[ak] *Università di Bologna, Dipartimento di Fisica e Astronomia, v.le C. Berti-Pichat, 6/2, Bologna, 40127 Italy, http://www.fisica-astronomia.unibo.it/it*
[al] *Università di Genova, Via Dodecaneso 33, Genova, 16146 Italy*
[am] *Università di Napoli "Federico II", Dip. Scienze Fisiche "E. Pancini", Complesso Universitario di Monte S. Angelo, Via Cintia ed. G, Napoli, 80126 Italy*
[an] *Università di Pisa, Dipartimento di Fisica, Largo Bruno Pontecorvo 3, Pisa, 56127 Italy*
[ao] *Università di Salerno e INFN Gruppo Collegato di Salerno, Dipartimento di Fisica, Via Giovanni Paolo II 132, Fisciano, 84084 Italy*
[ap] *Università La Sapienza, Dipartimento di Fisica, Piazzale Aldo Moro 2, Roma, 00185 Italy*
[aq] *Universitat Politècnica de Catalunya, Laboratori d'Aplicacions Bioacústiques, Centre Tecnològic de Vilanova i la Geltrú, Avda. Rambla Exposició, s/n, Vilanova i la Geltrú, 08800 Spain*
[ar] *Universitat Politècnica de València, Instituto de Investigación para la Gestión Integrada de las Zonas Costeras, C/ Paranimf, 1, Gandia, 46730 Spain*
[as] *Université de Strasbourg, IPHC, 23 rue du Loess, Strasbourg, 67037 France, http://https://www.unistra.fr/index.php?id=accueil*
[at] *APC, Université Paris Diderot, CNRS/IN2P3, CEA/IRFU, Observatoire de Paris, Sorbonne Paris Cité, 75205 Paris, France*
[au] *University Mohammed I, Faculty of Sciences, BV Mohammed VI, B.P. 717, R.P. 60000 Oujda, Morocco*
[av] *University of Amsterdam, Institute of Physics/IHEF, PO Box 94216, Amsterdam, 1090 GE Netherlands*
[aw] *University of Catania, Dipartimento di Fisica ed Astronomia di Catania, Via Santa Sofia 64, Catania, 95123 Italy*
[ax] *University of Johannesburg, Department Physics, PO Box 524, Auckland Park, 2006 South Africa*
[ay] *University of Pisa, DIMNP, Via Diotisalvi 2, Pisa, 56122 Italy*
[az] *University Würzburg, Emil-Fischer-Straße 31, Würzburg, 97074 Germany*
[ba] *Utrecht University, Department of Physics and Astronomy, PO Box 80000, Utrecht, 3508 TA Netherlands*

ABSTRACT: The Hamamatsu R12199-02 3-inch photomultiplier tube (PMT) is the photodetector chosen for Phase 1 of the KM3NeT neutrino telescope. About 7000 PMTs have been tested for dark count rate, timing spread and spurious pulses. For a sub-sample the quantum efficiency, the gain, the peak to valley ratio and the magnetic field effects have also been measured.

KEYWORDS: Photomultiplier; KM3NeT; Neutrino Telescope

Contents

1 Introduction

KM3NeT is a large research infrastructure that will consist of a network of deep-sea neutrino detectors in the Mediterranean Sea [1–3]. The main scientific goals are neutrino astro-particle physics, study of astrophysical objects by detecting their high-energy neutrino emission, and neutrino oscillation physics, investigation of neutrino properties by measuring atmospheric neutrinos. The KM3NeT location in the deep sea offers interdisciplinary opportunities for continuous, real-time measurements, e.g. for marine biology, oceanography or environmental sciences. The high-energy neutrino telescope of KM3NeT (Astroparticle Research with Cosmics in the Abyss, ARCA) will be located off-shore Capo Passero, Italy, 3500 m below the sea level. The low-energy neutrino telescope of KM3NeT (Oscillation Research with Cosmics in the Abyss, ORCA) will be located off-shore Toulon, France, 2500 m below the sea level.

Both arrays are made of thousands of Digital Optical Modules (DOMs). The DOMs, 18 per string, are arranged along flexible strings kept vertical by a submerged buoy. The strings are grouped in building blocks of 115 units. The complete ARCA telescope will consist of two building blocks; ORCA of one block, with smaller horizontal and vertical spacing. During the first stage of the KM3NeT construction (Phase 1) 24 strings for the ARCA and 6 strings for the ORCA detectors, respectively, will be installed. The DOMs will detect the Cherenkov light emitted in the sea from charged particles originating from neutrino interactions. Each DOM consists of 31 3-inch PMTs inside a 17-inch diameter glass sphere. The timing accuracy and the photon counting capability are the main parameters that determine the detector event reconstruction accuracy. The measurement of the arrival times of photons on the PMTs is crucial since it affects the accuracy of the event reconstruction. The charge estimate is based on the Time over Threshold (ToT) values of the PMT pulses and the number of hit PMTs on each DOM. The accuracy of this estimation affects the reconstructed energy resolution. Dark count rate and out of time pulses can also affect the telescope performance.

It is well known that the performance of a photomultiplier tube is subject to variation due to magnetic fields that can change the trajectories of the photo-electrons and also of secondary electrons. Since PMTs installed into optical modules of an underwater detector can change their orientation because of movements of the structures due to sea currents, the influence of the Earth's magnetic field must be investigated. Magnetic shielding is regularly used to reduce magnetic effects and make the response of the PMT independent of its orientation.

The requirements [1] for the main characteristics of the KM3NeT PMTs are summarized in Table 1. The Hamamatsu R12199-02 PMT [4] is the photodetector chosen for Phase 1 of the KM3NeT project. It is a 80 mm diameter hemispherical PMT with 10 dynodes and standard bi-alkali photocathode, see Fig. 1

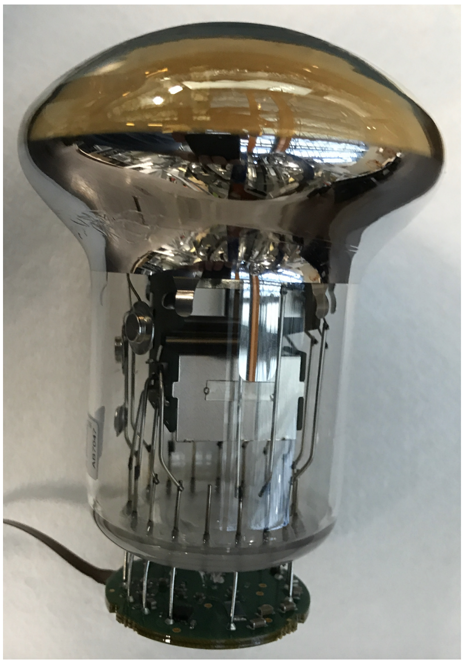

Figure 1. Hamamatsu 3-inch R12199-02 PMT.

The paper is organized as follows: in Section 2 the setup and the method used for the measurement of the Quantum Efficiency (QE) are discussed; in Section 3 the calibration of the gain and ToT dependence is shown for a sub-sample; in Section 4 the results from the test of about 7000 PMTs are discussed; finally in Section 5 the PMT performance as a function of its angle with respect to the Earth's magnetic field is summarized.

2 Quantum efficiency measurements

The photocathode quantum efficiency is measured in DC-mode, without any amplification. The whole dynode structure and the anode are connected using a dedicated base. A typical voltage of

Photocathode diameter	>72 mm
Nominal Voltage for gain 3x10^6	900-1300 V
Quantum Efficiency at 470 nm	> 18%
Quantum Efficiency at 404 nm	> 25%
Transit Time Spread (FWHM)	< 5 ns
Dark count rate (0.3 s.p.e. threshold, at 20°C)	2000 cps max
Prepulses between -60 ns and -10 ns	1.5% max
Delayed pulses between 15 ns and 60 ns	5.5% max
Late afterpulses between 100 ns and 10 μs	15% max

Table 1. Requirements from the KM3NeT neutrino telescope for the main PMT characteristics. N.B. cps stands for counts per second.

280 V is applied with respect to the photocathode. The PMT is illuminated with a Xenon lamp whose light passes through a monochromator. The photocurrent is measured by a picoammeter. The light intensity is determined using a reference photodiode calibrated by Hamamatsu in the wavelength range of 200 - 800 nm in steps of 10 nm with a precision of 0.1%. Reference measurements are repeated each hour. The scheme of the test setup for QE measurements is shown in Figure 2. The quantum efficiency is calculated as the ratio between PMT and photodiode photocurrents weighted with the known QE of the photodiode. QE is measured in the wavelength range of interest 280 - 700 nm in steps of 5 nm. More details on the method and on the possible systematics can be found in [5].

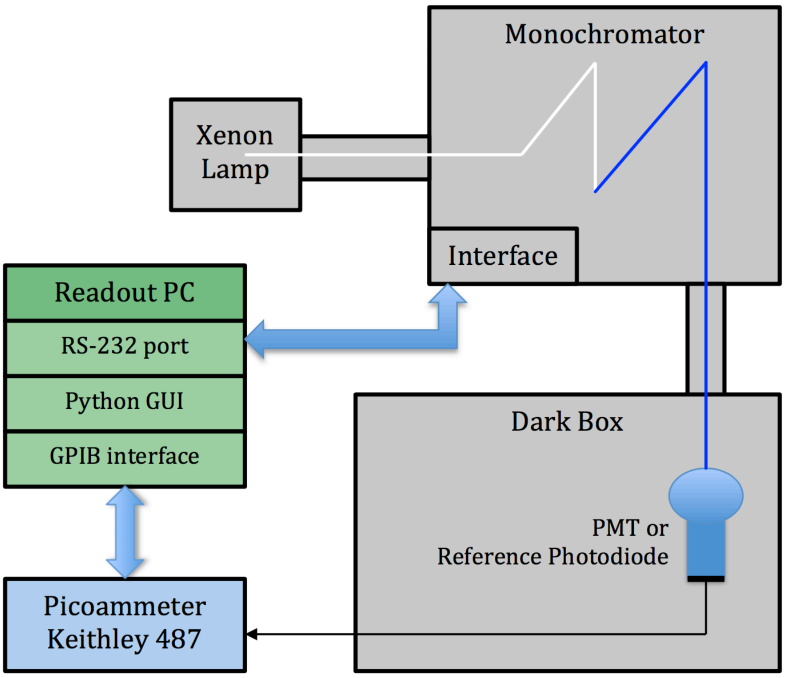

Figure 2. Scheme of the test setup for photocathode quantum efficiency measurements.

Photocathode QE was measured for 56 PMTs. The results are presented in Figure 3. Green lines show QE curves for individual PMTs; red curve is the mean value with standard deviation at each measured wavelength. For the wavelengths indicated in the KM3NeT specifications, QEs with standard deviations are: $(26.9 \pm 1.2)\%$ (@404 nm) and $(21.6 \pm 1.5)\%$ (@470 nm). The results are in agreement with the requirements.

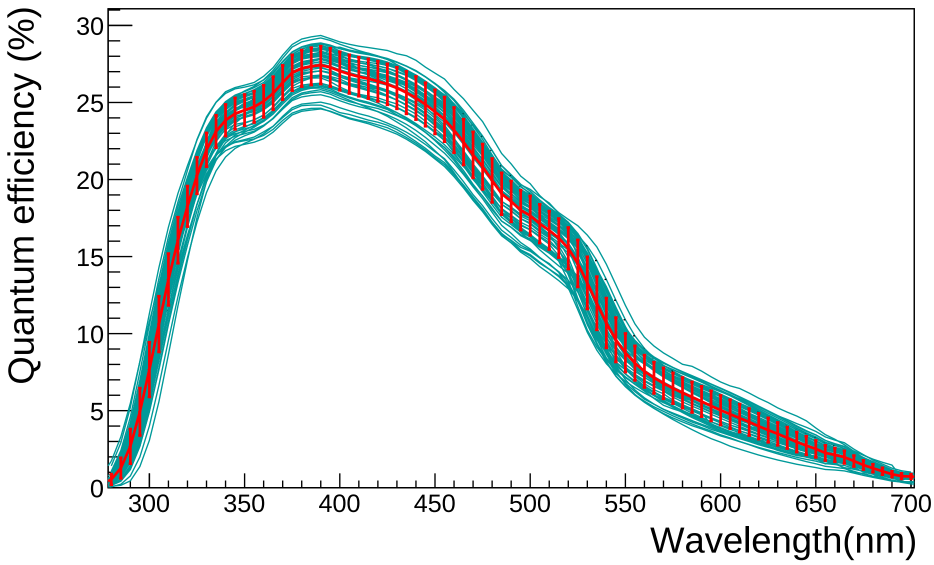

Figure 3. Photocathode Quantum Efficiency measurements as a function of the wavelength for 56 PMTs. The red curve shows the mean value with standard deviation at each measured wavelength.

3 Gain and Time-over-Threshold calibration

Hamamatsu provides a high voltage (HV) value for each PMT to achieve the nominal gain of 3×10^6. Gain is defined and measured by Hamamatsu as the ratio between anode and photocathode currents. In KM3NeT application, PMTs are not used in current, but in pulse mode. The majority of the detected pulses are due to single photo-electron (s.p.e.). A charge distribution of s.p.e. pulses is shown in Figure 4. The first peak is the so called pedestal, the baseline signal from the PMT in the absence of photon induced pulses; the red line is a Gaussian fit to the s.p.e. distribution. The PMT gain is a mean value of the fit expressed in units of number of electrons. The gain is defined as follow

$$gain = (spemean - pedmean) \times (v_{gain}/50) \times timestep/ampgain/e$$

where $spemean$ is the mean value of s.p.e distribution; $pedmean$ is the mean value of the pedestal; v_{gain} is the ADC scale expressed as Volts per ADC channel; 50 (expressed in Ohm) is the ADC load resistor; $timestep$ is the sampling time step in seconds; $ampgain$ is the amplification of the PMT; $e = 1.6022 \times 10^{-19}$ coulombs. For the plot in Figure 4, the following standard sets were used: $v_{gain} = 2.21 \times 10^{-3}$ Volts per ADC channel; $timestep = 10^{-9}$ s; $ampgain = 10$; $(spemean - pedmean) \simeq 125$ ADC channels. The corresponding gain is then 3.45×10^6.

Given the different methods to measure the gain, differences in nominal voltages are expected. Therefore, a method of HV tuning in order to get the nominal gain has been developed.

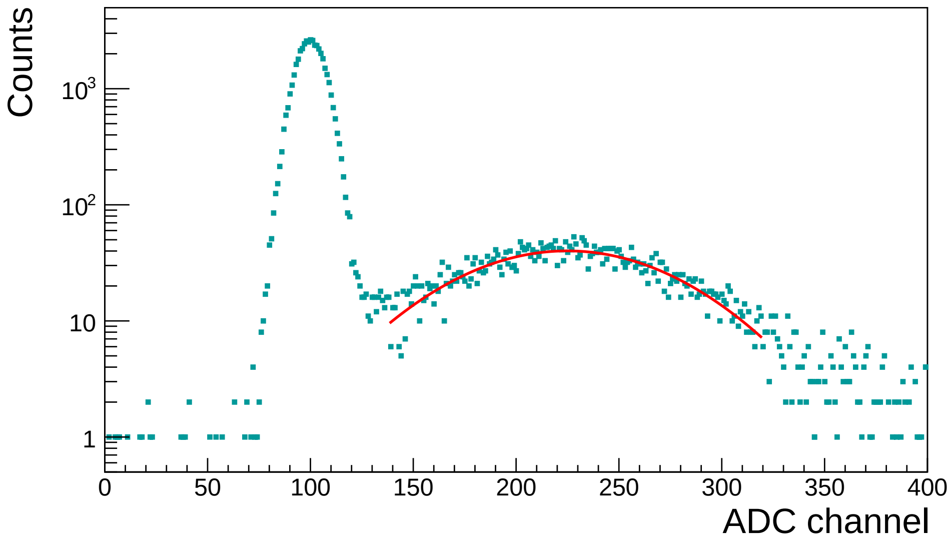

Figure 4. Single photo-electron charge distribution for a typical PMT. The red line shows the Gaussian fit to the s.p.e. distribution.

The nominal HV was measured for a sub-set of PMTs with resistive bases having a high-voltage division ratio of 3 between photocathode and first dynode, and of 1 between all other dynodes. The bases have throughout connectors providing safe inserting of PMTs flying leads. In a dark box the whole PMT surface is illuminated by fast LED pulses (460 nm central value with a 800 ns FWHM) at 1 kHz frequency. Light from the pulser is delivered to the dark box via an optical fiber. A diffusor is installed at the fiber output at a distance of ~1 m from the PMTs. The pulser amplitude is tuned to obtain a mean number of ~0.1 photon per pulse detected by the PMT, whose signal, amplified ten times, is sent to a LeCroy Waverunner 6100 oscilloscope. The latter is triggered with the sync signal from the pulser and the waveforms of PMT signals are saved with a sampling rate of 1×10^9 samples per second. The gain is calculated integrating the signal within a gate of 20 ns and fitting the distribution with a Gaussian function. Measurements of the gain are performed at seven different voltages around the HV provided by Hamamatsu with steps of 25 V. These results are used to fit the gain-HV linear dependence in a double logarithmic scale. The nominal HV corresponding to a gain of 3×10^6 is calculated from the fit with 1 V precision.

For the operation inside KM3NeT DOMs, PMTs are soldered with Cockcroft-Walton bases equipped with current amplifiers [6]. Maximal values (amplitudes) of the amplified signals are proportional to the charge of the initial pulse. Amplified signals have long trailing tails with lengths proportional to amplitudes. S.p.e. pulses after the amplification have an amplitude of ~500 mV. A tunable threshold discriminator on the base forms a rectangular ToT signal from the amplified analogue signal, which is sent to the Central Logic Board (CLB) of the DOM for digitization. In normal operation, only ToT signals are sent and the base dissipates only 30 mW power. There is also a possibility to read out the amplified analogue signal. In this case the power consumption increases, but this feature allows for threshold and ToT calibration in the laboratory where the power consumption is not critical. Both analogue and ToT are generated as differential signals. An example is shown in Figure 5.

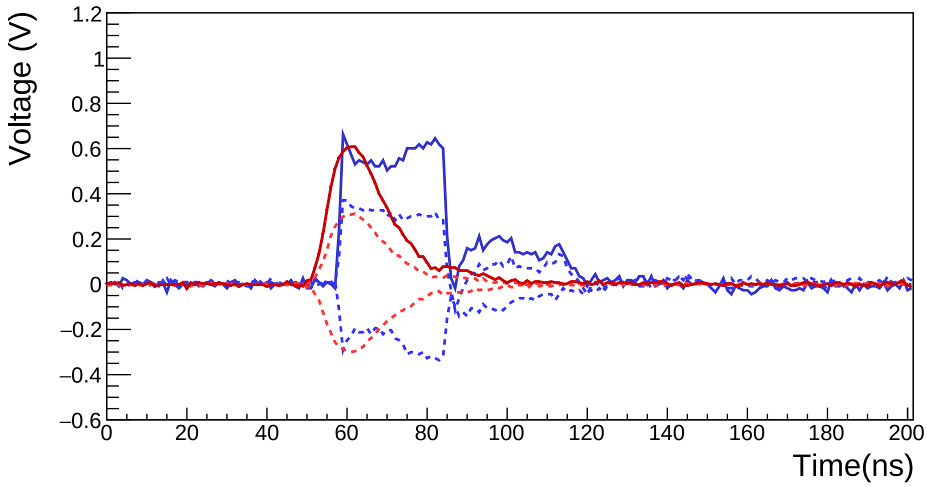

Figure 5. Analogue (red curves) and ToT (blue curves) signals from PMT base. The dashed lines shows the differential signal, while the continuous one the total signal.

A sub-sample of 66 PMTs was equipped with resistive bases to perform gain calibration, peak-to-valley ratio measurement and threshold-ToT calibration. In Figure 6-left the histogram with the gain slopes is shown. The nominal HVs for 3×10^6 gain derived from these measurements were compared with those provided by Hamamatsu. The difference between these two values is presented in Figure 6-right. There is a systematic difference that can be explained with the different methods used for gain measurement. The measured peak-to-valley ratio is shown in Figure 7.

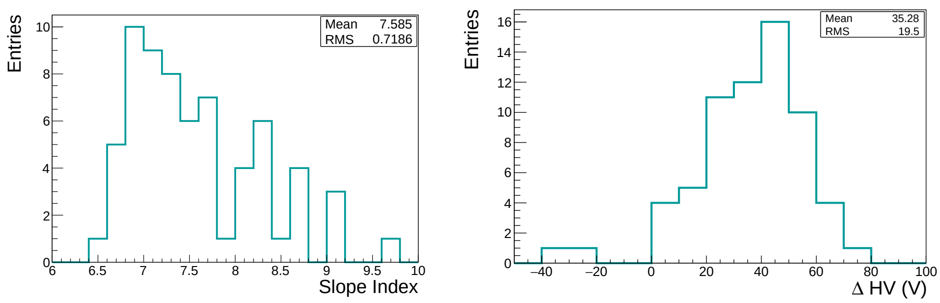

Figure 6. Left: Gain slope ; Right: Difference between measured high voltages and those provided by Hamamatsu for 3×10^6 gain.

Five out the 66 calibrated PMTs were soldered with active bases and threshold-ToT calibration was performed as follows. New nominal HVs were applied and a few s.p.e. data sets were taken with different thresholds set by encoders on bases. The mean value of the amplitude distributions from these measurements should correspond to 3×10^6 electrons charge. This mean value was derived from a Gaussian fit. Thresholds were determined as minimal values from the same distributions, and then expressed as a fraction of s.p.e. divided by mean value. The value for the threshold encoder corresponding to the 0.3 s.p.e. nominal threshold was calculated from the linear fit of the encoder-threshold dependence. Then the final measurement at nominal HV and nominal threshold was performed. The derived ToT distribution was fitted with a gaussion function. The obtained mean ToT value of 26.4 ns is the nominal ToT for single photo-electrons at 3×10^6 gain and with a threshold of 0.3 s.p.e.

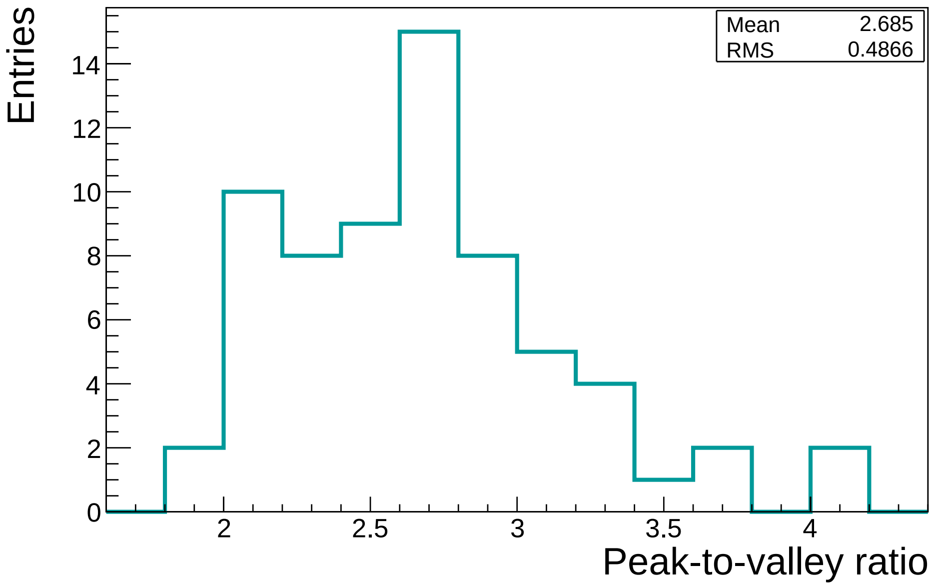

Figure 7. Peak-to-Valley ratio for a sub-sample of 66 PMTs.

4 Measurement of spurious pulses

A special device, dubbed DarkBox, has been developed [7] and it is shown schematically in Figure 8. It consists of a wooden box and removable trays designed to hold PMTs under test. A time-calibrated electrical cabling system was realised to connect PMTs to the data acquisition system placed outside the box, maintaining for all PMTs the same time signal delay. A picosecond accuracy laser and a calibrated optical splitting system are used to illuminate all PMTs in single photo-electron condition. Details on the mechanics, the electronics and the laser calibration system as well as its performance can be found in [7].

In this section we summarize the results obtained by testing 6960 PMTs.

The accurate, but time consuming, HV tuning procedure described in Section 3 cannot be applied for the tests. Therefore, it was decided to use the reference ToT value of 26.4 ns with a threshold at 0.3 s.p.e. as an indirect observable to equalize the PMT gains at 3×10^6. The HV for all PMTs is calibrated for the mass production in order to have the peak value of the time over

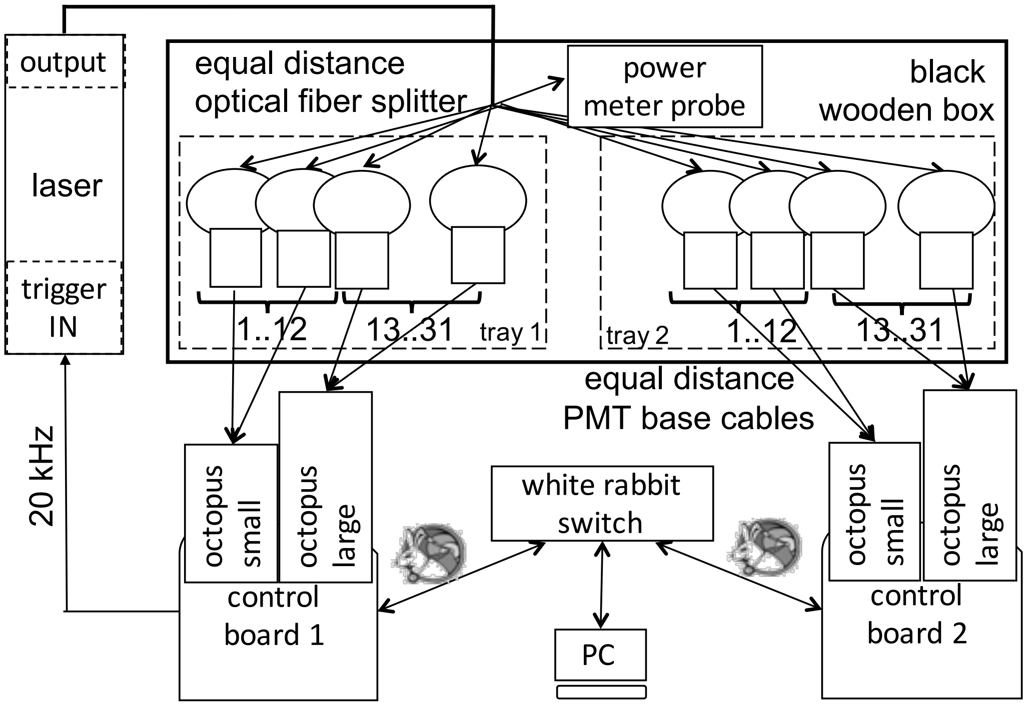

Figure 8. DarkBox experimental setup scheme [7].

threshold distribution at 26.4 ns, for a single photo-electron signal. We will refer to these high voltage as "tuned HV".

During a run with laser, the ToT distribution of the first hit is collected. The first hit is expected in a time window depending on the White Rabbit switch synchronization. This distribution has a peak in the range 26-27 ns confirming the reliability of the automatic HV calibration procedure.

The results discussed in the following sections have been obtained with tuned HV.

Note that for KM3NeT applications the anode is directly coupled to an external circuit, i.e. negative high voltage is used. In this case, optimal and stable performance can be obtained if precautions are taken to minimize any electrical discharges between the PMT and the holder. We adopted a solution by applying directly to the outside of the photomultiplier tubes the same insulating varnish as used for the high voltage bases [8].

4.1 Dark counts

In a PMT, noise pulses can be defined as anode output pulses not connected to a light event [9]. The dark counts are random noise pulses that can be measured at the anode of a PMT even in total darkness. The most significant source of random noise for a PMT is the spontaneous thermionic emission of electrons by the photocathode. Pulses that result from this process correspond mainly to a single photo-electron. The rate at which these pulses are observed is proportional to the area of the photocathode, and varies considerably between different photocathode materials. Bialkali photocathodes (as those used in KM3NeT PMTs) have the lowest ratio per unit of area. Another source of dark pulses is the natural radioactivity in the structure of the PMT itself. The most important components are usually ^{40}K and Th contained in the glass envelope. A beta particle emitted in radioactive decays will give rise to a flash of Cherenkov radiation that can produce photo-electrons emission from the photocathode [9].

Once the PMTs are fed with the tuned HV, dark count rates are monitored for 9 hours. During this time PMTs recover from the initial exposure to the light and the dark count rate stabilizes. The final rate is measured as the average value over the last 100 s of the run for each PMT. It is worth mentioning that PMTs with a dark count rate above 2000 cps are measured twice. This procedure, though time consuming, is mandatory to get rid of the residual instabilities induced by the material surrounding the PMT. The results are shown in Figure 9. The average dark count rate is 1289 cps, while the fraction of PMTs below 2000 cps is 92.9%.

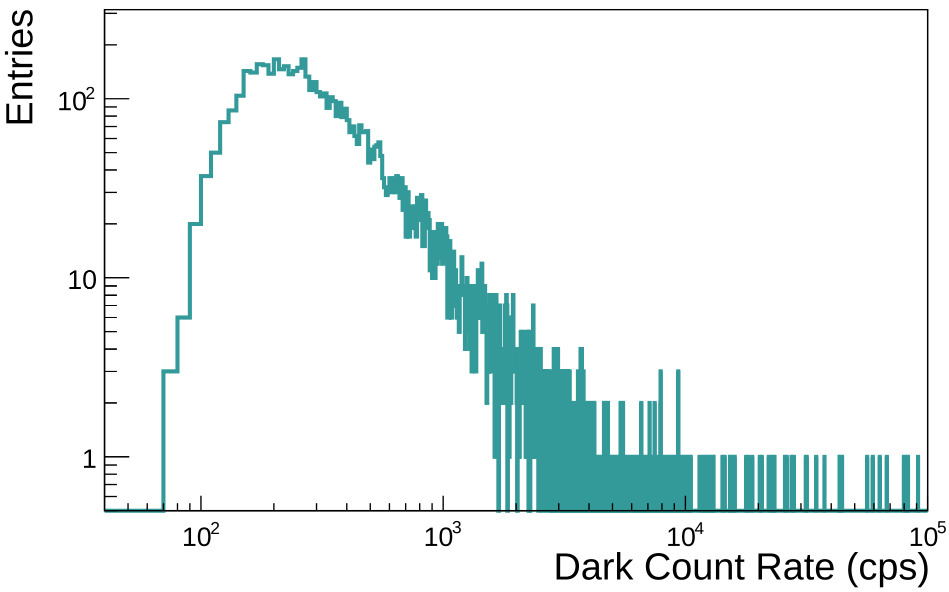

Figure 9. Dark Count rate for the whole sample analysed.

The effect of the artificial light on the dark count rate was also studied. Two different artificial light sources were considered: fluorescent tube lamps and LED lamps.

The dark count rate for six PMTs was measured in the DarkBox after several weeks of darkening. For all of them the measured dark count rate was below 200 cps.These PMTs were exposed for two hours to a fluorescent tube lamp light before the dark count rate measurement started. It took about a week of darkening to stabilize the dark count rate at the value previously measured. The same measurement was performed after a two hour exposure to a LED lamp light[1]. It took 4 hours to stabilize the dark count rate at the value previously measured.

4.2 Measurement of PMT time characteristics and of spurious pulses

Unlike dark counts, spurious pulses are time-correlated with the main PMT response to light events. Indeed, they can be early or delayed by a characteristic time with respect to the electron transit time through the PMT. They are usually classified in prepulses, delayed pulses and afterpulses. After the

[1]LED lamps with color in the range 3000-6000 K lead to similar results.

time needed for darkening a ten-minute-long run was performed with PMTs illuminated by a laser emitting at 470 nm. Its trigger frequency was set to 20 kHz and the light output tuned in order to operate PMTs in single photo-electron regime, (0.1 p.e. per pulse). These data were analysed to estimate PMT timing performances and quantify spurious pulses.

Timing characteristics

Time characteristics of PMTs are measured by detecting and analyzing the so called first photon hits, i.e. pulses detected in the window [T_0, T_0 + 200 ns], where T_0 is the calculated arrival time of laser photons on the PMT surface. First hits must have no hits before them in the defined time window. The time of arrival distribution of the first hits is shown in Figure 10. The earliest high peak of the distribution corresponds to the PMT transit time summed to the cable delay.

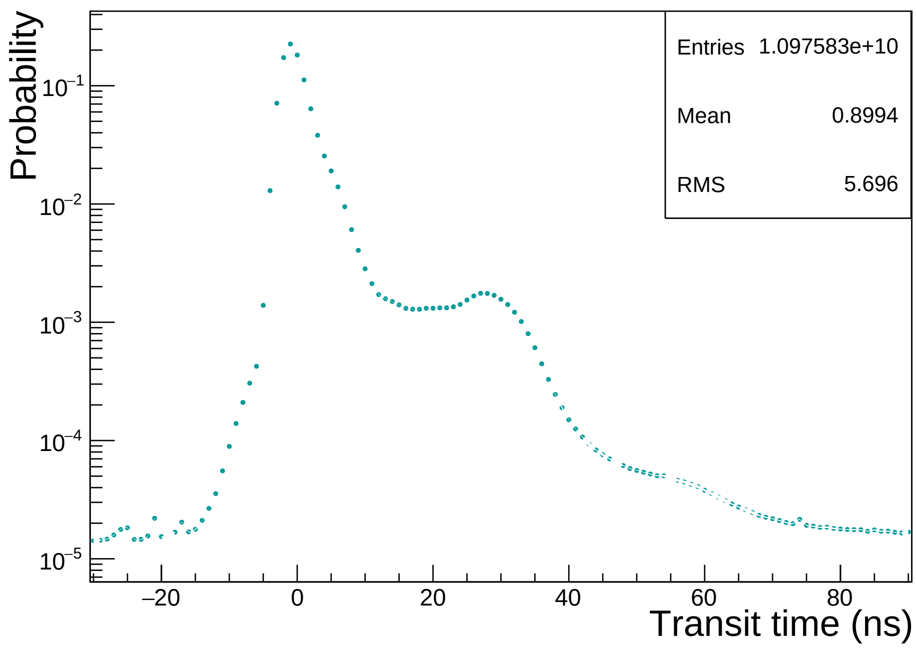

Figure 10. Average distribution of time of arrival of first hits for the whole sample.

The value of the transit time is determined as the centre of the bin with the maximum counts. The transit time spread (TTS) is defined as the FWHM of the main peak. Since the histogram binning is 1 ns, the error on FWHM is 1.4 ns. The results are shown in Figure 11 and indicate that TTS values are all below 5 ns.

Determination of prepulses and delayed pulses.

Prepulses arise from a direct photo-effect on the first dynode, due to photons that pass through the photocathode without interactions [10]. Prepulses are hence detected as the response of the PMT to a light event, but they appear before the typical arrival time of the main pulse, see Figure 10. For a 3-inch PMT the prepulse arrival time is in the range 10-16 ns before the main pulse. However, we followed a more conservative approach and considered the range 10-60 ns before the main pulse. The percentage of prepulses is defined as the ratio of the hits in the window

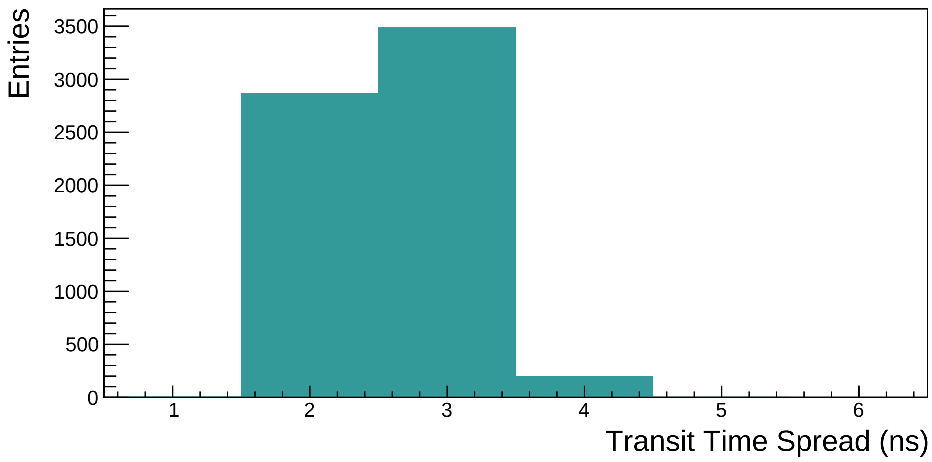

Figure 11. Transit Time Distribution spread for the whole sample.

$[T_{\mathrm{peak}} - 60.5\ \mathrm{ns}, T_{\mathrm{peak}} - 10.5\ \mathrm{ns}]$ over the number of the first hits; T_{peak} corresponds to the centre of the maximum bin (transit time peak).

The distribution of the prepulses measured for the tested PMTs is shown in Figure 12. 98.8% of the total sample has a prepulse fraction below 1.5%. The average prepulse fraction is 0.2%.

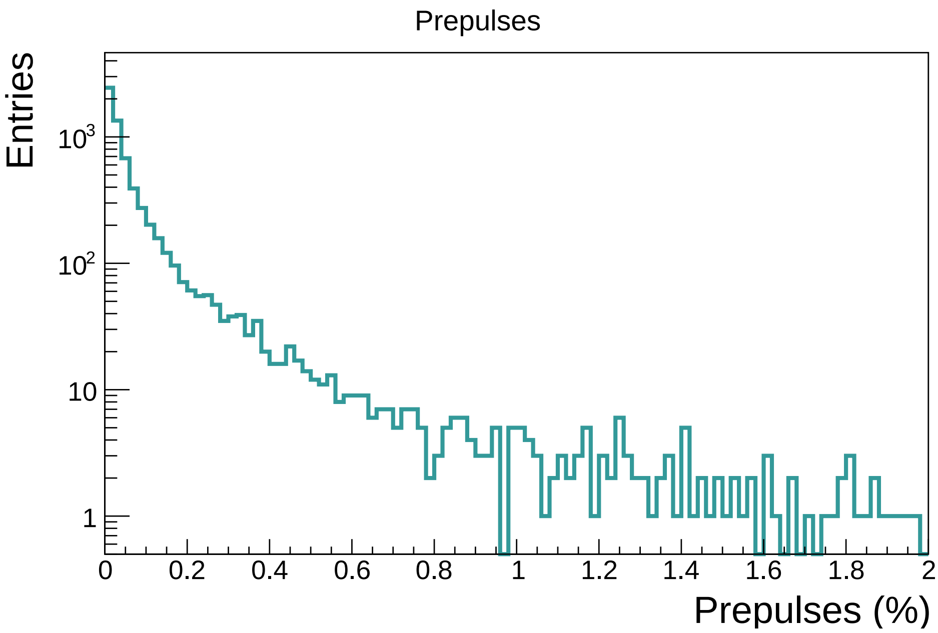

Figure 12. Prepulse distribution for the whole sample.

Delayed pulses are caused by elastic scattering of photo-electrons on the first dynode (D1) [10]. A photo-electron hitting the first dynode may be backscattered without liberating any secondary electron. Backscattered photo-electrons on the first dynode are decelerated by the electric field and then accelerated again towards it, giving secondary electrons. Thus, also delayed pulses are detected as the response of the PMT to a light event. Delayed pulses do not have a random time distribution, but they tend to accumulate around a time that is twice the photo-cathode to D1 transit time. Therefore, the falling edge of the main peak in Figure 10 is softened by the delayed pulses. The peak of delayed pulses, due to elastic scattering of the electrons on the dynodes, is observed in Figure 10 at about 30 ns after the main peak. The percentage of delayed pulses has been calculated as the ratio of the first hits in the window $[T_{\text{peak}} + 15.5\ \text{ns}, T_{\text{peak}} + 60.5\ \text{ns}]$ over the number of all first hits.

The distribution of the delayed pulses measured for the tested PMTs is shown in Figure 13. 98.5% of the total sample has a delayed fraction below 5.5%. The average delayed pulse fraction is 3.2%.

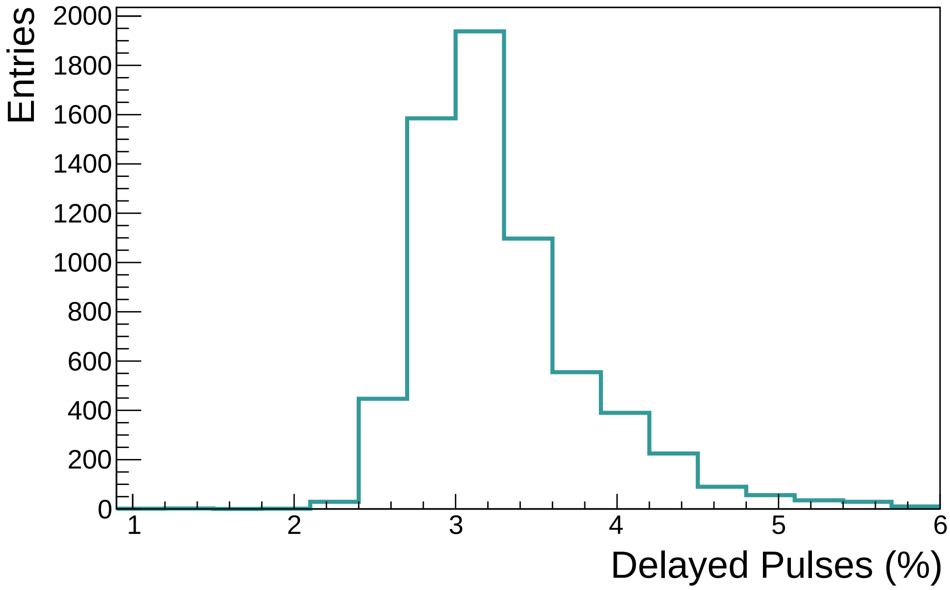

Figure 13. Delayed pulse distribution for the whole sample.

Determination of afterpulses

Afterpulses are noise pulses that can follow the main PMT response to a detected light event. One mechanism that can give rise to short delay afterpulses is the emission of light from the stages of the multiplier structure, which goes towards the photocathode where it can produce further photo-electrons. In general, PMTs exhibit Type I afterpulses in the time window 10-80 ns after the primary pulse [4]. Long delay afterpulses are commonly defined as Type II. They are caused by residual gases that can be ionized by the passage of electrons in the space between the photocathode to the first dynode and also through the multiplier structure. The positive ions that are formed will drift in the reverse direction and some can find a path back to the photo-cathode. Because the drift velocity of the positive ions is relatively low, the time they take to return to the photo-cathode can range from hundreds of nanoseconds to tens of microseconds. It also depends on the type of ions, on the position where they are generated and on the supply voltage.

Afterpulses are defined as hits with a first hit before them in a time window of 10 μs. The used front-end electronics does not allow for a good separation for the consecutive hits with a time difference $\lesssim$ 10 ns [2]. For 3-inch PMTs Type I afterpulses arrive $\leq$ 20 ns after the first hits, so their quantification is not possible with the current setup.

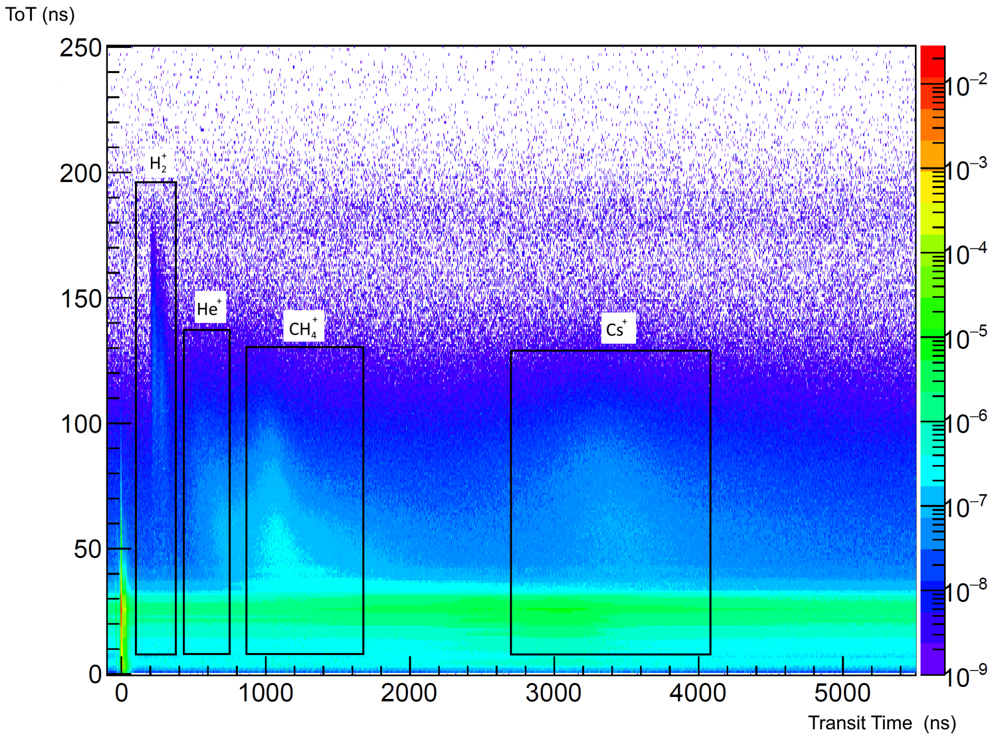

Figure 14. ToT as a function of the first hit time. The peaks corresponding to the signal induced by different ions are also indicated.

Considering the Type II afterpulse time distribution, for 3-inch PMTs two peaks at about 1 μs and 3 μs can be distinguished, as shown in Figure 14. These peaks are due to the residual gases inside the PMT. Given the typical drift velocity of each ion, the first one is presumably produced by CH_4 ions, the second one by Cs ions. Other peaks below 1 μs are due to hydrogen and helium ions.

The percentage of Type II afterpulses is determined as the ratio of afterpulses in the time window [T_{peak} + 100.5 ns, T_{peak} + 10 μs] over the number of first hits.

The percentages of spurious pulses of all types are eventually corrected taking into account the dark noise hits that contaminate both first hits and spurious pulse distributions.

The distribution of the afterpulses measured for the tested PMTs is shown in Figure 15. 92.4% of the total sample has an afterpulse fraction below 15%. The average afterpulse fraction is 7.1%.

4.3 Summary of the results

Following the results discussed in the previous Sections and the constraints shown in Table 1, it turned out that 93% of the measured PMTs complied with the requirements.

[2]Signal discrimination with 0.3 p.e. threshold concatenates both impulses to a single long one

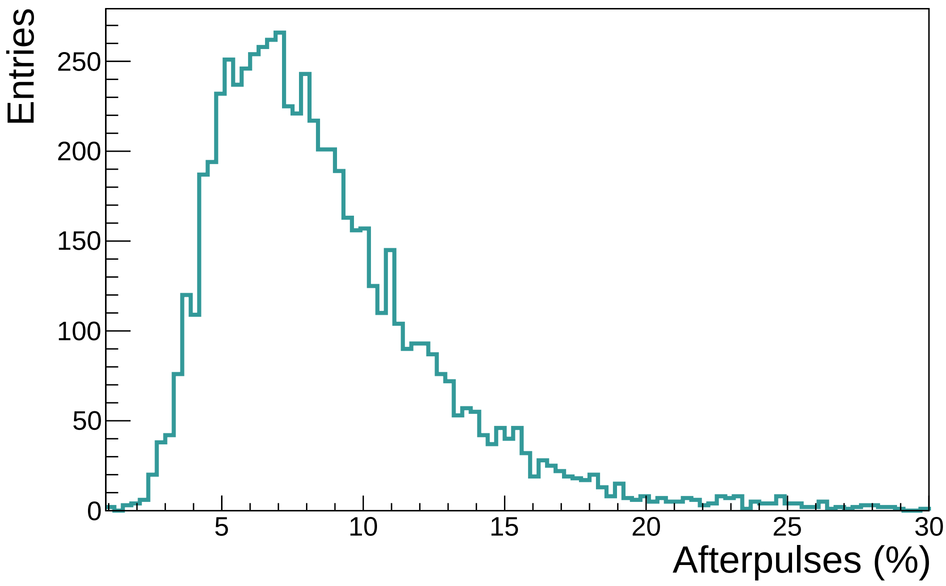

Figure 15. Afterpulse distribution for the whole sample analysed.

Variable outside the acceptance windows	Fraction of the events
Afterpulses	35.9%
Darkcounts	24.6%
Darkcounts+Afterpulses	13.3%
Delayed pulses	5.6%
Prepulses+Delayed pulses	4.4%
Darkcounts+Afterpulses+Prepulses	3.2%
Darkcounts+Afterpulses+Delayed pulses+Prepulses	3.0%
Darkcounts+Afterpulses+Delayed pulses	3.0%
Darkcounts+Prepulses	2.4%
Darkcounts+Prepulses+Delayed pulses	1.5%
Prepulses	1.5%
Prepulses+Afterpulses	0.73%
Afterpulses+Delayed pulses	0.44%
Prepulses+Afterpulses+Delayed pulses	0.43%

Table 2. Sources that caused the rejection of the PMTs. Note that the subsets are not overlapping and that percentages are calculated with respect to the rejected sample.

The sources that caused the rejection of a PMT are summarized in Table 2. Afterpulses and/or dark count rates account for about 75% of the rejected PMTs.

5 Measurement of Earth's magnetic field effects

Earth's magnetic field affects the PMT response deflecting the trajectories of the photo-electrons drifting from photocathode to first dynode, and also trajectories of secondary electrons in the dynode chain. Influences on such trajectories can have strong impacts on detection efficiency, timing and charge properties of the PMT. Since PMTs installed into optical modules of an underwater detector can change their orientation because of movements of the structures due to sea currents, the influence of Earth magnetic field must be investigated. Magnetic shielding is indeed largely used to reduce magnetic effects and make the response of the PMT orientation independent.

PMT response was measured while varying the orientation and inclination to the Earth's magnetic field. A light-tight dark box ($1 \times 0.5 \times 0.5$ m^3) able to rotate with respect to the vertical axis (steps of 1°) and to change its inclination (steps of 10°) was constructed for this purpose. No magnetic material was used, only PVC and Aluminium. A pulsed laser (PicoQuant PDL 800-B) with a 410 nm laser head, which can emit light pulses as short as 50 ps FWHM, was used as light source. The laser light was split and sent through multimode optical fibers to the PMT under test and to a second PMT kept as monitor of the intensity. An optical diffuser (Thorlabs (D1-C50) [11]), with a circular, flat intensity distribution within a 50° angle of divergence, provided homogeneous illumination over the PMT photocathode.

The location of the test box was carefully selected in order to ensure the uniformity of the Earth magnetic field within an area surrounding the box of at least 1 m. The magnitude of the magnetic field in this area was measured to be 40 μTesla.

The reference system used for these measurements is shown in Figure 16.

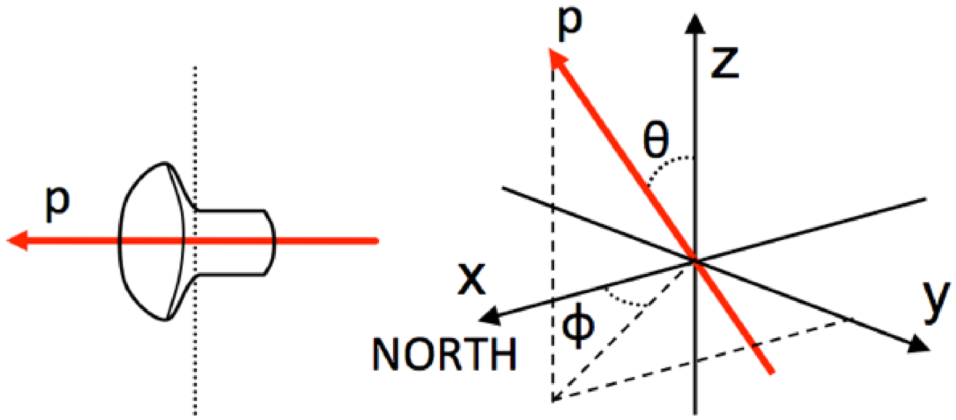

Figure 16. On the left: PMT axis in measurements (p). On the right: polar angle (θ) and azimuthal angle (ϕ)

Measurements were performed with a PMT surrounded by a cage made with 1-mm diameter mu-metal (a nickel-iron alloy with very high relative magnetic permeability [12]). The cage is a 68×68 mm^2 mesh, enough to avoid shadow effects on the PMT photocathode surface. An average magnetic field reduction factor of 4 was measured inside the cage.

θ	50° naked	50° shielded	90° naked	90° shielded	130° naked	130° shielded
Det. eff.	12.0%	10.1%	11.9%	6.8%	23.3%	6.7%
Gain	4.1%	2.8%	3.0%	1.6%	5.1%	1.8%
TTS	8.1%	5.0%	4.0%	1.7%	3.3%	1.5%

Table 3. Maximum variation of the detection efficiency (Det. Eff.) Gain, and TTS by rotating 360° horizontally the PMT at three inclinations θ.

One 3-inch PMT was tested by measuring the dependence of detection efficiency, gain and TTS on the azimuthal angle (ϕ). Measurements were performed for three different vertical orientations of the PMT: 50° upwards (θ = 50°), horizontal (θ= 90°) and 50° downwards (θ=130°). Figure 17 shows an example of gain measurement at θ = 130°. The maximum values of variation measured for each of the three different vertical positions, with and without the magnetic shield are summarized in Table 3. These variations were calculated as the percentage of the difference between the maximum and the minimum value, divided by the maximum.

For the 3-inch PMTs, the impact of Earth's magnetic field is negligible. The largest effect is found on the detection efficiency but not so high to justify the use of a magnetic shielding in the design of optical modules with 3-inch PMTs.

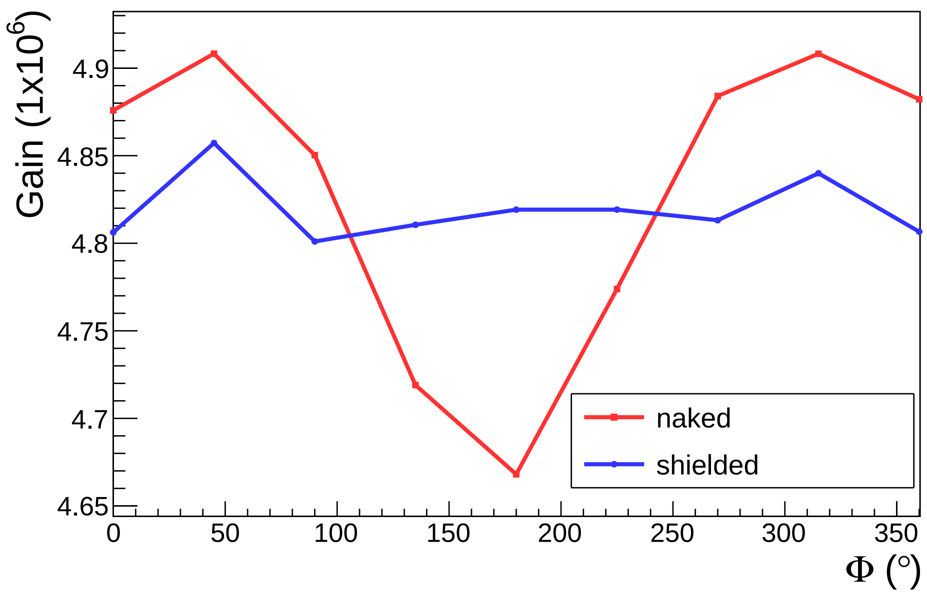

Figure 17. Azimuthal angle dependence of the gain for a 3-inch PMT oriented downwards at θ = 130°, in the case of naked (red line) and shielded (blue line) PMT.

Long term measurements performed so far on a detection unit operating at the KM3NeT-It off-shore site show rotations on the horizontal plane lower than 20° for DOMs. Within such angular range, the measured variation on unshielded PMTs was always below 8% for detection efficiency and below 3% for gain and TTS .

6 Conclusions

About 7000 Hamamatsu PMTs, type R12199-02, to be used for Phase 1 of the KM3NeT have been characterized. The main parameters, such as dark counts, TTS, prepulses, delayed and afterpulses have been measured for the whole sample. It turned out that 93% of the tested PMTs complied with the requirements.

For a sub-sample of about 60 PMTs the QE, the gain and the peak-to-palley ratio were measured and the results found in agreement with the expectations. These measurements were also used for the gain and ToT calibrations. A threshold at 0.3 s.p.e. was fixed and the nominal ToT of 26.4 ns was derived from the calibrations.

Finally, the effect of the different orientation of the PMT with respect to the Earth magnetic field was also measured. It turned out that the response of 3-inch PMTs has small dependence on the Earth magnetic field. Therefore, unlike the large PMT case [13], the use of a mu metal cage is not necessary.

Acknowledgments

The authors acknowledge the financial support of the funding agencies: Agence Nationale de la Recherche (contract ANR-15-CE31-0020), Centre National de la Recherche Scientifique (CNRS), Commission Européenne (FEDER fund and Marie Curie Program), Institut Universitaire de France (IUF), IdEx program and UnivEarthS Labex program at Sorbonne Paris Cité (ANR-10-LABX-0023 and ANR-11-IDEX-0005-02), France; 'Helmholtz Alliance for Astroparticle Physics' funded by the Initiative and Networking Fund of the Helmholtz Association, Germany; The General Secretariat of Research and Technology (GSRT), Greece; Istituto Nazionale di Fisica Nucleare (INFN), Ministero dell'Istruzione, dell'Università e della Ricerca (MIUR), Italy; Agence de l'Oriental and CNRST, Morocco; Stichting voor Fundamenteel Onderzoek der Materie (FOM), Nederlandse organisatie voor Wetenschappelijk Onderzoek (NWO), the Netherlands; National Authority for Scientific Research (ANCS), Romania; Plan Estatal de Investigación (refs. FPA2015-65150-C3-1-P, -2-P and -3-P, (MINECO/FEDER)), Severo Ochoa Centre of Excellence and MultiDark Consolider (MINECO), and Prometeo and Grisolía programs (Generalitat Valenciana), Spain.

References

[1] S. Adrián-Martínez *et al.* [KM3Net Collaboration], "Letter of Intent for KM3NeT2.0", J. Phys. G: Nucl. Part. Phys. 43 (2016) 084001.

[2] S. Adrián-Martínez et al. [KM3NeT Collaboration], "Deep sea tests of a prototype of the KM3NeT digital optical module", Eur. Phys. J. C **74**, no. 9, 3056 (2014).

[3] S. Adrián-Martínez *et al.* [KM3NeT Collaboration], "The prototype detection unit of the KM3NeT detector", Eur. Phys. J. C **76** (2016) no.2, 54.

[4] Hamamatsu Photonics Photomultiplier Tubes Handbook https://www.hamamatsu.com

[5] B. Herold, O. Kalekin , J. Reubelt, "PMT characterisation for the KM3NeT project", Nucl. Instr. & Meth. in Phys. R. A 639 (2011) 70.

[6] P. Timmer, E. Heine and H. Peek, "Very low power, high voltage base for a photo multiplier tube for the KM3NeT deep sea neutrino telescope," JINST **5** (2010) C12049. doi:10.1088/1748-0221/5/12/C12049

[7] C. M. Mollo *et al.*, "A new instrument for high statistics measurement of photomultiplier characteristics", JINST **11** (2016) no.08, T08002 doi:10.1088/1748-0221/11/08/T08002 [arXiv:1604.03922 [physics.ins-det]].

[8] S. Adrián-Martínez *et al.* [KM3NeT Collaboration], "A method to stabilise the performance of negatively fed KM3NeT photomultipliers", JINST **11** (2016) no.12, P12014 http://dx.doi.org/10.1088/1748-0221/11/12/P12014.

[9] G. F. Knoll, Radiation detection and measurements, John Wiley Sons, Inc. (1999).

[10] B.K. Lubsandorzhiev et al., "Photo-electron backscattering in vacuum phototubes", Nucl.Instrum.Meth. A567 (2006) 12-16.

[11] website: www.thorlabs.com

[12] Institute for Theoretical and Experimental Physics, Moscow, http://www.itep.ru

[13] S. Aiello, E. Leonora, A. Grimaldi, G. Leotta, D. Lo Presti, N. Randazzo, D. Sciliberto and V. Sipala, "Influence of the Earth's magnetic field on large area photomultipliers," IEEE Trans. Nucl. Sci. **59** (2012) 1259. doi:10.1109/TNS.2012.2189245